ARL-TR-9543 • SEP 2022

Tuning Flap Control Authority from High-Fidelity, Coupled CFD/RBD Virtual Fly-Outs

by Bradley T Burchett, Jubaraj Sahu, and Benjamin Gruenwald

Approved for public release: distribution unlimited.

NOTICES

Disclaimers

ARL-TR-9543 ● SEP 2022

Tuning Flap Control Authority from High-Fidelity, Coupled CFD/RBD Virtual Fly-Outs

Bradley T Burchett and Benjamin Gruenwald
DEVCOM Army Research Laboratory

Jubaraj Sahu
Oak Ridge Associated Universities

REPORT DOCUMENTATION PAGE	*Form Approved* *OMB No. 0704-0188*

1. REPORT DATE *(DD-MM-YYYY)* September 2022	**2. REPORT TYPE** Technical Report	**3. DATES COVERED (From - To)** 1 June–1 September 2022

4. TITLE AND SUBTITLE Tuning Flap Control Authority from High-Fidelity, Coupled CFD/RBD Virtual Fly-Outs	**5a. CONTRACT NUMBER** **5b. GRANT NUMBER** **5c. PROGRAM ELEMENT NUMBER**
6. AUTHOR(S) Bradley T Burchett, Jubaraj Sahu, and Benjamin Gruenwald	**5d. PROJECT NUMBER** **5e. TASK NUMBER** **5f. WORK UNIT NUMBER**
7. PERFORMING ORGANIZATION NAME(S) AND ADDRESS(ES) DEVCOM Army Research Laboratory ATTN: FCDD-RLW-WD Aberdeen Proving Ground, MD 21005	**8. PERFORMING ORGANIZATION REPORT NUMBER** ARL-TR-9543
9. SPONSORING/MONITORING AGENCY NAME(S) AND ADDRESS(ES)	**10. SPONSOR/MONITOR'S ACRONYM(S)** **11. SPONSOR/MONITOR'S REPORT NUMBER(S)**

12. DISTRIBUTION/AVAILABILITY STATEMENT

Approved for public release: distribution unlimited.

13. SUPPLEMENTARY NOTES

ORCID IDs: Bradley T Burchett,0000-0002-1934-0537; Benjamin Gruenwald, 0000-0003-3968-5070

14. ABSTRACT

Several methods are applied to tune the zero angle-of-attack (AoA) force and moment contribution of a trailing edge flap actuator on a projectile with strongly roll-dependent aerodynamics. Rather than relying on force/moment predictions from computational fluid dynamics (CFD) in steady flight conditions, a coupled CFD/RBD simulation is used to predict the vehicle response over time to frequency-rich, independent input signals on all four actuators. The actuator positions, predicted forces, and moments are processed through a custom regression algorithm that sorts the inputs and regressors into 16 bins based on aerodynamic bank. The zero AoA force and moment contribution of each flap is estimated at each of the 16 bank angles resulting in 64 estimates of each coefficient at each flight condition. These 64 estimates are used to determine a harmonic model of the corresponding force/moment term over a full roll cycle. The amplitudes of the resulting harmonic models are used to tune the corresponding amplitudes in the existing aerodynamic model.

15. SUBJECT TERMS

onboard sensors, projectile aerodynamics, trajectory reconstruction, initial conditions, dual spin, Weapons Sciences

16. SECURITY CLASSIFICATION OF:			**17. LIMITATION OF ABSTRACT**	**18. NUMBER OF PAGES**	**19a. NAME OF RESPONSIBLE PERSON**
					Bradley T Burchett
a. REPORT	**b. ABSTRACT**	**c. THIS PAGE**			**19b. TELEPHONE NUMBER (Include area code)**
Unclassified	Unclassified	Unclassified	UU	42	(410) 306-0792

Standard Form 298 (Rev. 8/98)
Prescribed by ANSI Std. Z39.18

Contents

List of Figures

List of Tables

1. Introduction

The design of a guided projectile for long-range precision targeting requires a combination of high-fidelity modeling, precise sensing, state estimation, optimal guidance, and advanced control design. Some tradeoffs can be made between the disciplines; for example, less fidelity in aerodynamic modeling can be somewhat compensated by more expensive adaptive and robust control design. However, when a projectile is widely deployed, unit production cost can be reduced by employing cheaper sensors and controls while more thorough and precise modeling ensures program success.

Traditionally, aerodynamic modeling was accomplished through wind tunnel (WT) and flight tests.[1,2] Dynamic quantities such as damping constants were difficult in the WT, and poorly estimated prior to flight tests. Now that computational fluid dynamics (CFD) are widely used, steady-state aerodynamics can be precisely determined without WT or flight tests; however, the dynamic terms require more innovative tools. Recently coupled CFD/rigid body dynamics (RBD) simulations are becoming more prevalent as a means to estimate dynamic terms by performing a virtual "fly-out" of the vehicle.[3,4] Since the CFD codes directly supply the forces and moments as functions of time and vehicle state, most of the aerodynamic coefficients are easily found through a simple regression. Dynamic terms such as damping and actuator authority still require some additional insight that is provided by system identification theory.

The vehicle used in this study has been modeled extensively using several computational tools. A baseline aerodynamic model (AM) was developed by Vasile et al.[5] using DATCOM, Cart3D, and CFD++. Several assumptions were made to reduce the number of configurations tested in each of the computational environments. This study will demonstrate the validity of those assumptions, particularly the roll dependence and superposition applied to individual flap deflections. The baseline model is described in further detail in Section 2.4.

The vehicle was also subjected to extensive WT testing at Florida State University.[6] In a previous work[7] we proposed a method to tune the flap pitch authority terms for the full configuration at zero aerodynamic bank. Although the WT test matrix included six flap deflections ($\delta \in \{\pm 5, \pm 10, \pm 20\}^\circ$) the pitch experiments were performed at only two Mach numbers and two bank angles. Thus, the data set is far too sparse for global tuning over the (M, δ) flight envelope. Also, all four flaps were deflected in a symmetric fashion; therefore, individual contributions could not be easily isolated. Due to the expensive and time-consuming nature of WT testing, we turn to a numerical experiment to capture vehicle performance at a wide range of flight conditions.

Recent advances in system identification provide a means of designing input signals for flight tests such that all actuators are moved simultaneously, and their individual contributions are observable in the response.[8] By using this input signal design technique, we can contrive a numerical experiment where all four actuators are moved over a short time horizon and their individual contributions to the total forces and moments can be estimated.

This report will review a recently developed high-fidelity, coupled CFD/RBD simulation. We will then briefly review the design of multisine staircase inputs for system identification. After that we describe the sorting, regression, and global model fit in some detail. Finally, we discuss fusing the new estimates with an existing aerodynamic database. Results corresponding to each step of the process are presented in the relevant subsections of this report.

2. MATLAB/CFD++ Coupled Simulation

2.1 CFD Technique

The complete set of 3-D, time-dependent Navier–Stokes equations is solved in a time-asymptote manner to obtain converged steady-state solutions. A commercially available code, CFD++,[9,10] is used and the 3-D, time-dependent Reynolds-averaged Navier–Stokes (RANS) equations are solved using the following finite volume method:

$$\frac{\partial}{\partial t}\int_V \mathbf{W}dV + \oint[\mathbf{F} - \mathbf{G}] \cdot dA = \int_V \mathbf{H}dV \qquad (1)$$

where **W** is the vector of conservative variables, **F** and **G** are the inviscid and viscous flux vectors, respectively, **H** is the vector of source terms, V is the cell volume, and A is the surface area of the cell face.

Several techniques such as implicit scheme and relaxation are used to achieve faster convergence. Use of an implicit scheme circumvents the stringent stability limits suffered by their explicit counterparts, and successive relaxation allows update of cells as information becomes available and thus aids convergence. Second-order discretization was used for the flow variables and the turbulent viscosity equation. The turbulence closure is based on topology-parameter-free formulations. A realizable two-equation k-ϵ turbulence model[11] was used for the computation of turbulent flows. These models are ideally suited to unstructured bookkeeping and massively parallel processing due to their independence from constraints related to the placement of boundaries and/or zonal interfaces. The basic CFD solution technique described here is coupled with an RBD for simultaneous prediction of controlled and uncontrolled flights.

2.2 Coupled CFD/RBD/Flight Control System (FCS) Procedure

In the coupled CFD/RBD procedure, the forces and moments are computed every CFD time step and transferred to a six-degrees-of-freedom (6-DOF) module that computes the body's response to the forces and moments. The response is converted into translational and rotational accelerations that are integrated to obtain translational and rotational velocities and then integrated once more to obtain linear position and angular orientation. This coupled technique provides both the unsteady aerodynamics and the flight dynamics in an integrated manner. Figure 1 illustrates the coupled CFD/RBD workflow. Force and state values are passed to the MATLAB RBD module, which determines the rate of change of state variables and integrates forward in time. In turn the RBD module passes selected elements of the state vector to the FCS module, which computes control commands that pull actuator positions from the system state vector. The updated states and actuator positions are passed back to CFD++ for prediction of aerodynamic forces and moments at the next time step, and so on.

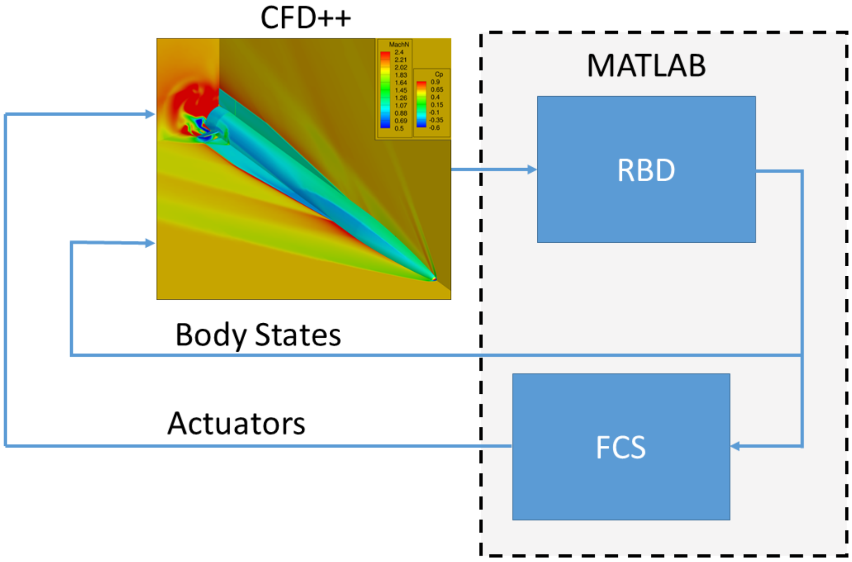

Fig. 1 Coupled CFD/RBD workflow

A time-accurate numerical approach is used in the coupled CFD/RBD simulations. This approach requires that the 6-DOF RBD be computed at each repetition of a flow solver. The CFD capability[9,10] used here solves the full Navier–Stokes equations and incorporates advanced boundary conditions and grid motion capabilities. For time-accurate simulations of coupled flights, a dual time-stepping procedure is generally used to achieve the desired time accuracy in the time-accurate solutions. The entire grid is moved to account for the motion of the projectile. To account for RBD, the grid point velocities were set as if the grid is attached to the rigid body with 6-DOF.

Typically, the coupled solution procedure requires three steps. First, we begin with a computation performed in the "steady-state mode" with the grid velocities prescribed to account only for the translational motion component of the complete set of initial conditions. At the second step, we also impose the angular orientations from the initial conditions. At this stage, spin is normally added. In the present study, we are interested in pitching motions only; thus, spin is set to zero. Computations are performed in a time-accurate mode for a desired number of time steps (500–1000). Converged solution from this second step provides the initial condition for the third step. In the third step, the remaining rotational velocity components (pitch and yaw) are added. The solution from the third step should correspond to the complete set of initial conditions that includes all translational and rotational velocity components and accounts for initial position and angular orientations. For simulations of controlled maneuvers (open- or closed-loop), a procedure that integrates flight control into the coupled CFD/RBD method is used.

2.3 MATLAB-Based 6-DOF

An in-house RBD that is completely based on MATLAB has been developed and implemented in the coupled procedure. In addition to using the MATLAB environment, we added two significant enhancements to the existing in-house simulation framework.

First, continuous states from all subsystems (plant, actuator, control laws) are concatenated in one long system state vector and integrated simultaneously for more realistic continuous time simulation. The current implementation provides for up to 300 continuous states; however, expansion is easily facilitated by modifications to the ".c-based" interface. To avoid difficulty compiling the MATLAB codes, we chose to make the MATLAB memory space completely volatile—requiring the state history to be stored entirely on the CFD++ side.

Second, actuator and control system state derivatives are sequestered to a subfunction to achieve modularity. Simulation users can provide their own actuator models and dynamic control systems without modifying the baseline CFD/RBD simulation engine.

The CFD++ simulation uses a 12-state input vector consisting of the vehicle position and mass center velocity in ground-fixed Cartesian coordinates, $\mathbf{X} = \{x \quad y \quad z\}$ and $\dot{\mathbf{X}} = \{\dot{x} \quad \dot{y} \quad \dot{z}\}$, respectively, the vehicle orientation expressed as the standard set of aircraft Euler angles ($\mathbf{\Theta} = \{\phi \quad \theta \quad \psi\}$), and the three body-fixed angular rates ($\boldsymbol{\omega} = \{p \quad q \quad r\}$). From these inputs it renders force/moment predictions in the ground-fixed frame.

The relationships between ground- and body-fixed coordinates are illustrated in Figs. 2 and 3.

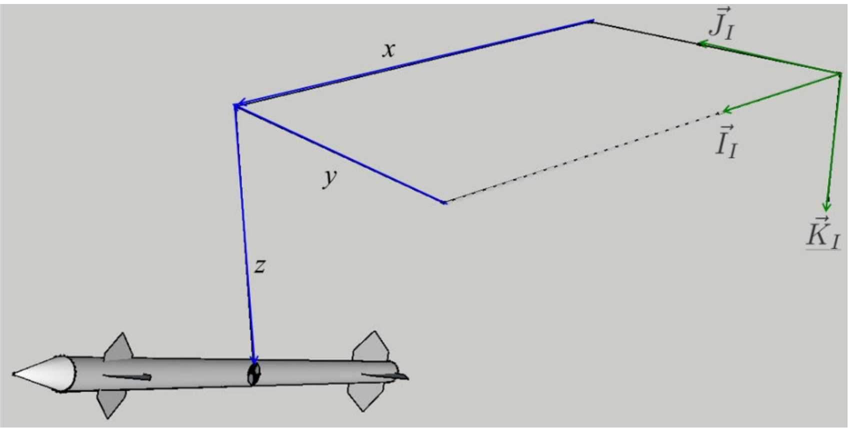

Fig. 2 Ground-fixed Cartesian coordinates for projectile center of gravity (cg) position defined

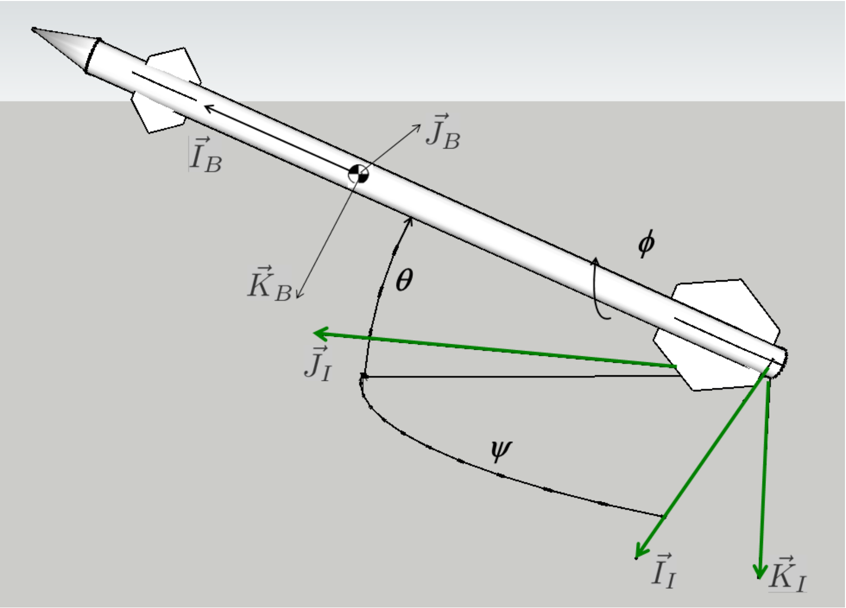

Fig. 3 Standard Euler angles defined

Our 6-DOF RBD model uses a standard state vector consisting of the concatenation of vehicle cg position in ground-fixed Cartesian coordinates, $\mathbf{X} = \{x \quad y \quad z\}$, orientation as the customary set of Euler angles, $\boldsymbol{\Theta} = \{\phi \quad \theta \quad \psi\}$, velocity in the body-fixed frame, $\mathbf{U} = \{u \quad v \quad w\}$, and body angular rates in the body frame, $\boldsymbol{\omega} = \{p \quad q \quad r\}$. Thus, the overall state is $\boldsymbol{\zeta} = \{\mathbf{X} \quad \boldsymbol{\Theta} \quad \mathbf{U} \quad \boldsymbol{\omega}\}$.

Since the CFD uses ground-fixed velocity, forces, and moments, the first step in the RBD simulation is to transform these quantities into the body frame. Given

$$\mathbf{T}_{i2b} = \begin{bmatrix} c_\theta c_\psi & c_\theta s_\psi & -s_\theta \\ s_\phi s_\theta c_\psi - c_\phi s_\psi & s_\phi s_\theta s_\psi + c_\phi c_\psi & s_\phi c_\theta \\ c_\phi s_\theta c_\psi + s_\phi s_\psi & c_\phi s_\theta s_\psi - s_\phi c_\psi & c_\phi c_\theta \end{bmatrix} , \tag{2}$$

the body-fixed velocity vector is found as:

$$\mathbf{U} = \mathbf{T}_{i2b}\dot{\mathbf{X}} , \tag{3}$$

the body-fixed force vector $\mathbf{F}^{\mathbf{RBD}} = \{X \quad Y \quad Z\}$ is given as:

$$\mathbf{F}^{\mathbf{RBD}} = \mathbf{T}_{i2b}\mathbf{F}^{\mathbf{CFD}} , \tag{4}$$

and the body-fixed moment vector $\mathbf{M}^{\mathbf{RBD}} = \{l \quad m \quad n\}$ is given as:

$$\mathbf{M}^{\mathbf{RBD}}{=}\mathbf{T}_{i2b}\mathbf{M}^{\mathbf{CFD}} . \tag{5}$$

The CFD force vector does not include gravity, which is found as:

$$\vec{\mathbf{F}}_{\boldsymbol{grav}} = \begin{Bmatrix} -s_\theta \\ s_\phi c_\theta \\ c_\phi c_\theta \end{Bmatrix} mg = \mathbf{T}_{i2b} \begin{Bmatrix} 0 \\ 0 \\ mg \end{Bmatrix} , \tag{6}$$

and simply added to render the total force on the projectile:

$$\mathbf{F}_{\boldsymbol{tot}} = \mathbf{F}^{\mathbf{RBD}} + \vec{\mathbf{F}}_{\boldsymbol{grav}} . \tag{7}$$

Once the required quantities are found in the body frame, the derivatives of the state vector follow a standard formulation:

$$\begin{Bmatrix} \dot{x} \\ \dot{y} \\ \dot{z} \end{Bmatrix} = \mathbf{T}_{i2b}^{T} \begin{Bmatrix} u \\ v \\ w \end{Bmatrix} \tag{8}$$

$$\begin{Bmatrix} \dot{\phi} \\ \dot{\theta} \\ \dot{\psi} \end{Bmatrix} = \mathbf{T}_{b2e} \begin{Bmatrix} p \\ q \\ r \end{Bmatrix} \tag{9}$$

$$\begin{Bmatrix} \dot{u} \\ \dot{v} \\ \dot{w} \end{Bmatrix} = \begin{Bmatrix} X/m \\ Y/m \\ Z/m \end{Bmatrix} - \mathbf{S} \begin{Bmatrix} u \\ v \\ w \end{Bmatrix} \tag{10}$$

$$\begin{Bmatrix} \dot{p} \\ \dot{q} \\ \dot{r} \end{Bmatrix} = [\mathbf{I}]^{-1} \left[\begin{Bmatrix} l \\ m \\ n \end{Bmatrix} - \mathbf{S}[\mathbf{I}] \begin{Bmatrix} p \\ q \\ r \end{Bmatrix} \right] \tag{11}$$

where

$$\mathbf{T}_{b2e} = \begin{bmatrix} 1 & s_\phi t_\theta & -c_\phi t_\theta \\ 0 & c_\phi & -s_\phi \\ 0 & s_\phi / c_\theta & c_\phi / c_\theta \end{bmatrix} \qquad \mathbf{S} = \begin{bmatrix} 0 & -r & q \\ r & 0 & -p \\ -q & p & 0 \end{bmatrix}, \tag{12}$$

and [**I**] is the 3-D body-fixed inertia tensor.

2.4 Roll-Dependent Aerodynamic Model

The vehicle in this study has long, low-aspect ratio fins that cause the aerodynamic forces and moments to be strongly roll dependent. In addition, the baseline AM predicts forces and moments in the “wind” frame as functions of aerodynamic bank and total angle-of-attack (AoA) rather than AoA and sideslip. Mathematically, we may write this as

$$\mathbf{F} = \mathbf{f}(\phi_a, \bar{\alpha}) \tag{13}$$

$$\mathbf{M} = \mathbf{g}(\phi_a, \bar{\alpha}) \tag{14}$$

where

$$\phi_a = \tan^{-1}(v/w) \tag{15}$$

and

$$\bar{\alpha} = \sqrt{\alpha^2 + \beta^2} \tag{16}$$

and

$$\alpha = \sin^{-1}\left(\frac{w}{\sqrt{u^2+v^2+w^2}}\right), \beta = \sin^{-1}\left(\frac{v}{\sqrt{u^2+v^2+w^2}}\right). \tag{17}$$

Force/moment coefficients are decomposed into contributions from the rigid aerodynamic surfaces $(.)^R$ and moveable aerodynamic surfaces $(.)^M$. Each component is predicted as a high-order polynomial in $\sin\bar{\alpha} = s_{\bar{\alpha}}$:

$$\begin{gathered} C_\vartheta^R = C_{\vartheta 0}^R(M,\phi) + C_{\vartheta 1}^R(M,\phi) s_{\bar{\alpha}} + C_{\vartheta 2}^R(M,\phi) s_{\bar{\alpha}}^2 + C_{\vartheta 3}^R(M,\phi) s_{\bar{\alpha}}^3 \\ + C_{\vartheta 4}^R(M,\phi) s_{\bar{\alpha}}^4 + C_{\vartheta 5}^R(M,\phi) s_{\bar{\alpha}}^5 \end{gathered} . \tag{18}$$

Vasile et al.[5] proposed that the forces and moments due to a deflected flap could be determined from the difference of predictions of the forces and moments on the total body with one flap deflected and the forces and moments with zero deflections. They further proposed that the force/moment model for an individual flap over a full roll cycle could be assembled from the force/moment prediction at zero aerodynamic bank as follows.

$$C_N^{M_1}(\delta,\phi) = C_N^{M_1}(0,\phi) + \left(C_S^{M_1}(\delta,0) - C_S^{M_1}(0,0)\right)\cdot\sin\phi_A + \left(C_N^{M_1}(\delta,0) - C_N^{M_1}(0,0)\right)\cdot\cos\phi_A \tag{19}$$

$$C_S^{M_1}(\delta,\phi) = C_S^{M_1}(0,\phi) + \left(C_S^{M_1}(\delta,0) - C_S^{M_1}(0,0)\right)\cdot\cos\phi_A - \left(C_N^{M_1}(\delta,0) - C_N^{M_1}(0,0)\right)\cdot\sin\phi_A \tag{20}$$

$$C_m^{M_1}(\delta,\phi) = C_m^{M_1}(0,\phi) + \left(C_m^{M_1}(\delta,0) - C_m^{M_1}(0,0)\right)\cdot\cos\phi_A + \left(C_n^{M_1}(\delta,0) - C_n^{M_1}(0,0)\right)\cdot\sin\phi_A \tag{21}$$

$$C_n^{M_1}(\delta,\phi) = C_n^{M_1}(0,\phi) - \left(C_m^{M_1}(\delta,0) - C_m^{M_1}(0,0)\right)\cdot\sin\phi_A + \left(C_n^{M_1}(\delta,0) - C_n^{M_1}(0,0)\right)\cdot\cos\phi_A \tag{22}$$

This assumption has two significant consequences. First, over a full roll cycle, each force/moment will have a maximum amplitude at some $\phi_A = n(\pi/2)$ for an integer value of *n*. Second, this maximum amplitude will be shared by the transverse forces (*N*, *S*) at a given deflection and likewise by the transverse moments (*m*, *n*) at a given δ. Both assumptions will be confirmed in the ensuing analysis.

As shown in Fig. 4a, the moveable aerodynamic surface (MAS)1 table may be applied for each of MAS2–MAS4 by simply incrementing the aerodynamic bank angle by $\pi/2$ for each MAS. For example, for side force:

$$C_S^{M_2}(\phi) = C_S^{M_1}\left(\phi + \frac{\pi}{2}\right), C_S^{M_3}(\phi) = C_S^{M_1}(\phi + \pi). \tag{23a,b}$$

$$C_S^{M_4}(\phi) = C_S^{M_1}(\phi + 3\pi/2) \tag{23c}$$

And for normal force:

$$C_N^{M_2}(\phi) = C_N^{M_1}\left(\phi + \frac{\pi}{2}\right), C_N^{M_3}(\phi) = C_N^{M_1}(\phi + \pi). \tag{24a,b}$$

$$C_N^{M_4}(\phi) = C_N^{M_1}(\phi + 3\pi/2) \tag{24c}$$

The wind frame is constant and oriented as shown with respect to the relative wind. Thus, the total force/moment for the airframe is a simple sum of components from RAS and MAS terms.

$$C_\vartheta^B = C_\vartheta^R + C_\vartheta^{M_1} + C_\vartheta^{M_2} + C_\vartheta^{M_3} + C_\vartheta^{M_4} \tag{25}$$

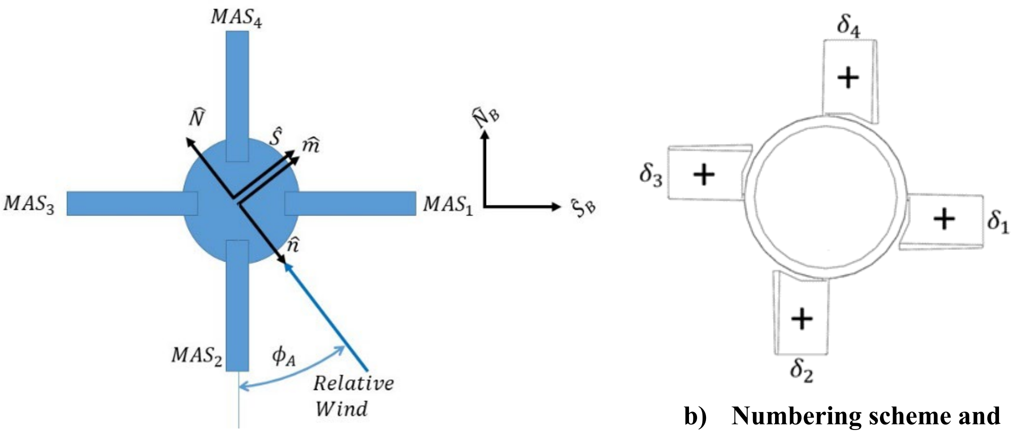

a) Wind and body frames with aerodynamic bank defined

b) Numbering scheme and sign convention for trailing edge flaps

Fig. 4 Reference frames for MAS deflection and buildup. Viewed from projectile base.

The focus of this work is to better characterize the zero AoA flap authority coefficients—namely, $C_{\vartheta 0}^{M_1}$, for $\vartheta \in \{N, S, m, n\}$. We capitalize on the relationships in Eqs. 23 and 24 and their moment counterparts to map simultaneous motion of all four MAS effectors back to a single bank varying term by setting up the regressor vectors accordingly. This is discussed at length in Section 4.2.

2.5 Numerical Integration

To limit the number of calls to the CFD solver and capitalize on the history of force/moment predictions, a third-order, Adams-Moulton numerical integration scheme was used. This method can be compactly written as

$$y_{n+1} = y_n + \frac{h}{12}(23\dot{y}_n - 16\dot{y}_{n-1} + 5\dot{y}_{n-2}) \tag{26}$$

$$y_{n+1} = y_n + \frac{h}{12}(5\dot{y}_{n+1} + 8\dot{y}_n - \dot{y}_{n-1}) \tag{27}$$

where y is the full system state vector, and h is the integration time step. Dot notation indicates the state–time derivative prediction from Eqs. 8–11 and auxiliary equations included in the control laws and actuator dynamics. The subscript n indicates the current time step, $n + 1$ is one step in the future, $n - 1$ is one step in the past, and so forth. The method is *implicit* because the state prediction at the next time step depends upon a derivative estimate at the next time step.

Equation 26 serves as a predictor step where the state at the next time step is predicted in order to estimate the state derivative $\dot{y}_{n+1}$ one step into the future. This future state derivative prediction will rely on the current force/moment predictions from CFD, so the algorithm suffers slightly from this approximation.

Equation 27 serves as a corrector step, using the one-step-ahead derivative prediction in conjunction with the current and one-step-ago predictions. This implicit predictor–corrector scheme was chosen as opposed to the explicit Adams-Bashforth in order to enhance the numerical stability of the integration.

Additional details on all aspects of the simulation are available in our previous publications.[3,4,9]

3. Orthogonal Multisine Staircase Inputs and System Identification

The virtual fly-out environment allows the user to test various control algorithms and prescribed maneuvers without the costly overhead of actual flight hardware and instrumentation. However, state-of-the-art parallel computing facilities still require about 100 h of actual time to compute 3 s of flight time. Thus, the computational experiment needs to be well designed prior to submitting to the supercomputer—trial and error would be far too costly. To design the numerical experiment well, we depend on system identification theory.

A key part of the experiment design is to choose input functions for the actuators, so that they are moved simultaneously over a short time horizon in such a way that their individual contributions are observable and separable. The input functions should move the vehicle enough to vary the transverse forces and moments; however, the vehicle states should remain near the initial flight conditions so that Mach number and altitude can be considered constant.

3.1 Orthogonal Multisine Inputs

Orthogonal multisine staircase inputs are an established method to achieve the previously stated goals. Optimized multisine inputs have been recently presented by Morelli and others. Here we will summarize the treatment of Morelli.[8]

Multisine inputs are simply a sum of harmonics as the name implies:

$$\mathbf{u} = \sum_{k \in \{1,2,\ldots,M\}} A\sqrt{P_k}\sin\left(\frac{2\pi kt}{T} + \phi_k\right) . \tag{28}$$

Since k is an integer, the minimum separation between harmonics is $(1/T)$ Hz. The highest frequency in Eq. 28 is $2\pi M/T$ rad/s and the lowest frequency is $2\pi M/T$ rad/s. The T and M should be chosen so that the spectrum of vehicle-free response dynamics is within this range.

When designing for multiple actuators, subsets of the harmonics in Eq. 28 are assigned to each actuator. A common technique is to interleave the harmonics. For instance, in the case with four actuators, one would choose

$$\begin{array}{ll} u_1 & k \in \{1,5,9,\dots\} \\ u_2 & k \in \{2,6,10,\dots\} \\ u_3 & k \in \{3,7,11,\dots\} \\ u_4 & k \in \{4,8,12,\dots\} \end{array}$$

One can easily show the mutual orthogonality of signals determined by Eq. 28 as follows. Consider two inputs where each contains a single harmonic

$$u_1 = \sin\left(\frac{2\pi k_1 t}{T} + \phi_1\right), u_2 = \sin\left(\frac{2\pi k_2 t}{T} + \phi_2\right), k_1 \neq k_2. \tag{29}$$

To show that the two signals are orthogonal, take the inner product, write the time vector as a discrete set ($t_i = i\Delta t$ and $T = (N-1)\Delta t$), and sum the product over one fundamental period

$$u_1^T u_2 = \sum_{i=0}^{N-1} \sin\left(\frac{2\pi k_1}{N-1} i + \phi_1\right) \sin\left(\frac{2\pi k_2}{N-1} i + \phi_2\right). \tag{30}$$

Using the identity

$$\sin(u)\sin(v) = \frac{1}{2}(\cos(u-v) - \cos(u+v)), \tag{31}$$

Eq. 30 becomes

$$u_1^T u_2 = \frac{1}{2}\sum_{i=0}^{N-1} \cos\left(\frac{2\pi(k_1-k_2)}{N-1} i + \phi_1 - \phi_2\right) - \frac{1}{2}\sum_{i=0}^{N-1} \cos\left(\frac{2\pi(k_1-k_2)}{N-1} i + \phi_1 - \phi_2\right) \tag{32}$$

and since the summation of any harmonic over the fundamental period is zero, both terms in Eq. 32 are zero. Thus, the four inputs designed using Eq. 28 and subsequent equations will be mutually orthogonal.

3.2 Phase Optimization

Signals designed using Eq. 28 with $\phi_k = \phi \ \forall \ k$ will have large amplitudes where the underlying harmonics are in phase with each other. These large amplitudes can have the deleterious effects of a) requiring deflections beyond physical limits and/or

b) causing the vehicle to depart too far from the desired nominal flight condition. The latter effect is only exacerbated when multiple actuators are commanded to large deflections simultaneously. Since ϕ_k are free variables in the design, they may be selected to minimize the largest amplitudes in each input. This is done by minimizing the relative peak factor (RPF) of each input by modifying the individual phases:

$$\min_{\phi_k} RPF(u(\phi_k)) = \frac{(\max(u)-\min(u))}{2\sqrt{2}\mathrm{rms}(u)}. \tag{33}$$

The minimization can be easily performed by a simplex method. Figure 5a and 5b illustrate the summation of harmonics before and after application of Eq. 33. However, the phase optimized signal in Fig. 5b has one fatal flaw—it begins at a large nonzero value. Since the actuator has finite bandwidth, this is physically impossible to implement. Thus, one final step is applied to shift the phase of all the harmonics an equal amount until the initial value of the input is close to zero. The result of such a shift is shown in Fig. 5c where the starting point is shifted about 0.3 s along the time axis. No large discontinuity in the actuator motion is required to use the signal in Fig. 5c.

The design outlined in Eq. 28 and subsequent equations is completely implemented in the SIDPAC function `mkmsswp.m`.

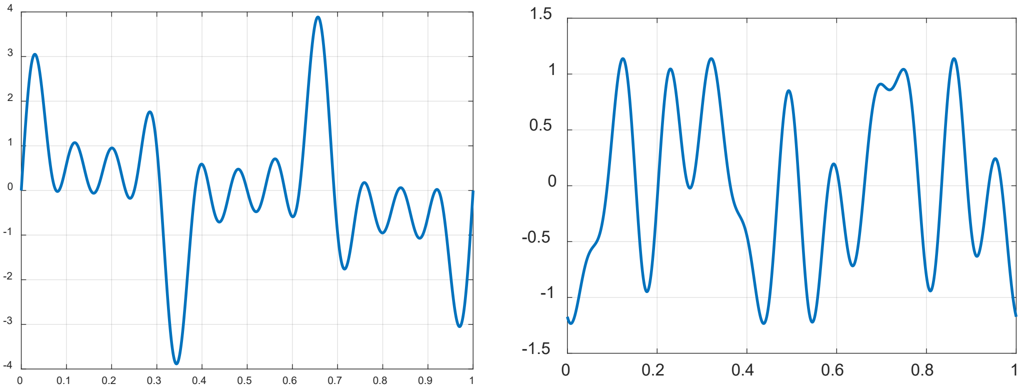

a) Sum of harmonics

b) With phase optimization

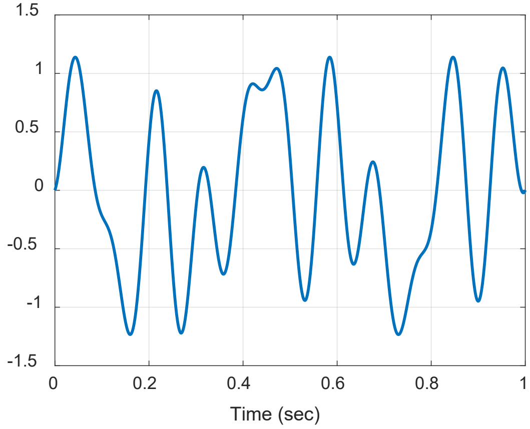

c) After shifting initial time to a node

Fig. 5 Orthogonal multisine design. Panel a) shows the sum of harmonics in phase resulting in large amplitudes. Panel b) shows the same sum with phases modified to minimize RPF. Panel c) shows the signal from panel b) with all phases shifted so that the deflection at time = 0 is zero.

3.3 Orthogonal Multisine Staircase Functions

Early attempts at system identification in the coupled environment with smooth signals such as those shown in Fig. 5 resulted in two problems. First, the coherence and conditioning of the regression was hindered by samples in the time history where the deflections are small. Second, the coefficients to be determined are actually a table of values at finite flap deflections—namely,

$$\boldsymbol{\delta} \in \pm\{0, 2, 5, 10, 15, 20, 25, 30\}^\circ \quad . \tag{34}$$

Thus, the input signal was redesigned so that the actuators would dwell at one of the finite deflections previously listed. In the latest iteration, we chose the set of deflections:

$$\boldsymbol{\delta} \in \{5, 10, 15, 20\}^\circ \quad . \tag{35}$$

Symmetry will be assumed for the negative deflections. In fact, the previous set defines the amplitudes of the final signals; therefore, negative deflections will be commanded, but will be lumped in with the corresponding positive counterpart by applying symmetry.

The orthogonal multisine functions presented previously can be converted to square waves simply be taking the signum of each harmonic prior to summation:

$$\mathbf{u} = \sum_{k\in\{1,2,\ldots,M)} A\sqrt{P_k}\,\mathrm{sign}\left(\sin\left(\frac{2\pi kt}{T} + \phi_k\right)\right). \tag{36}$$

For a simulation with a 3-s time horizon and a vehicle with natural frequencies between 4 and 19 rad/s, only eight harmonics are possible. Each input will use two of the possible eight. The final test signals for the largest deflection are shown in Fig. 6.

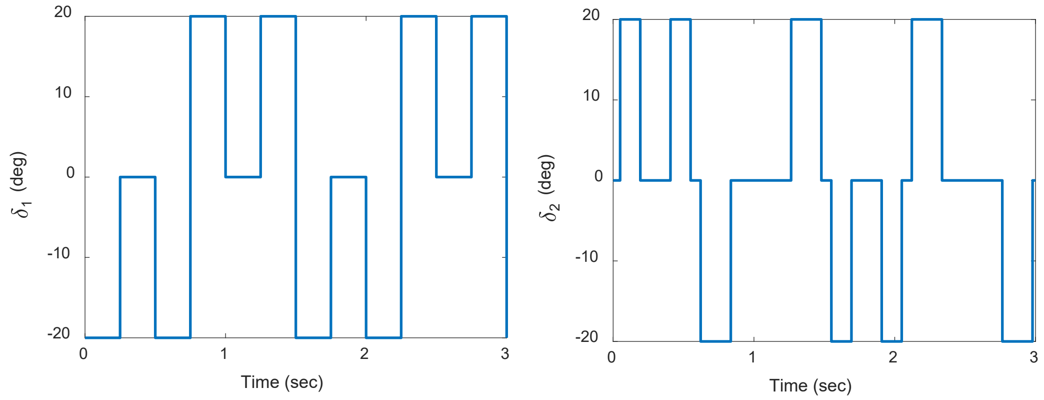

a) Actuator 1

b) Actuator 2

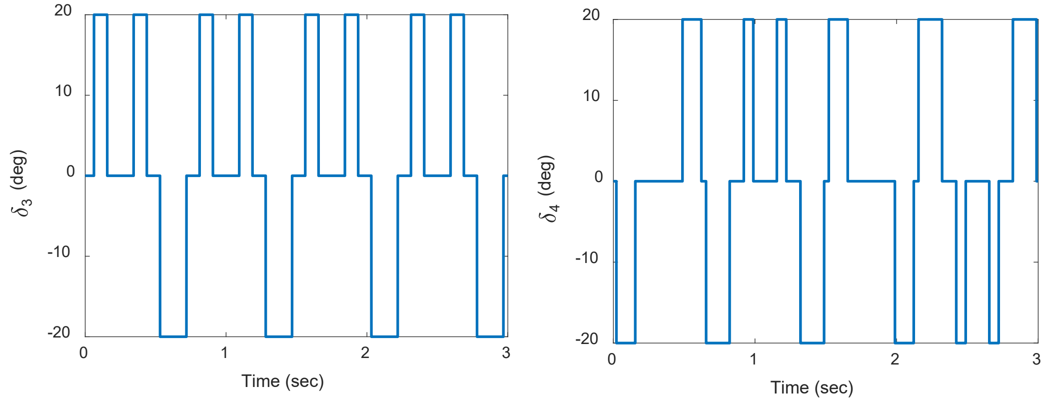

c) Actuator 3

d) Actuator 4

Fig. 6 Orthogonal staircase input signals for 20° of deflection

4. Post-Flight Data Reduction and Results

4.1 Basic Regression Analysis

The coupled CFD/RBD simulation provides the full state history plus forces and moments in the body frame at 2 kHz sampling for the 3-s flight. A sample force and moment history is shown in Fig. 7. After examining the moment data, we decided to perform smoothing on it using the `lsmoo` function in SIDPAC with a window length of 50 samples.

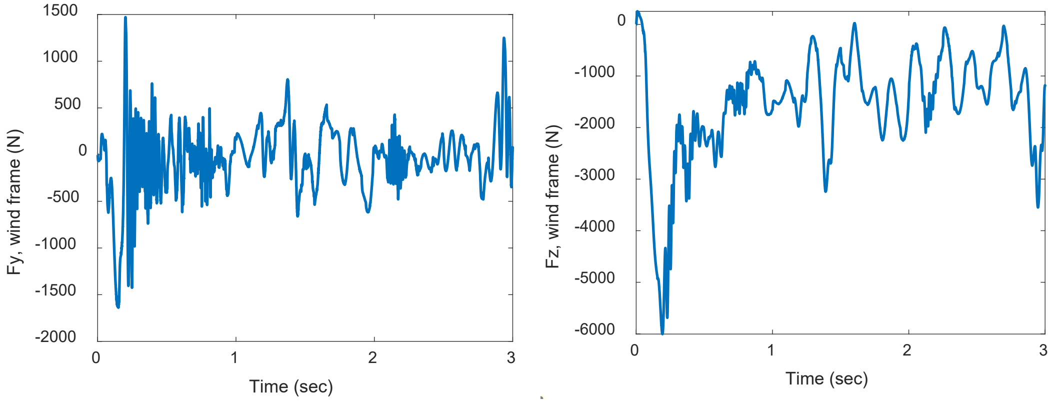

a) Side force

b) Normal force

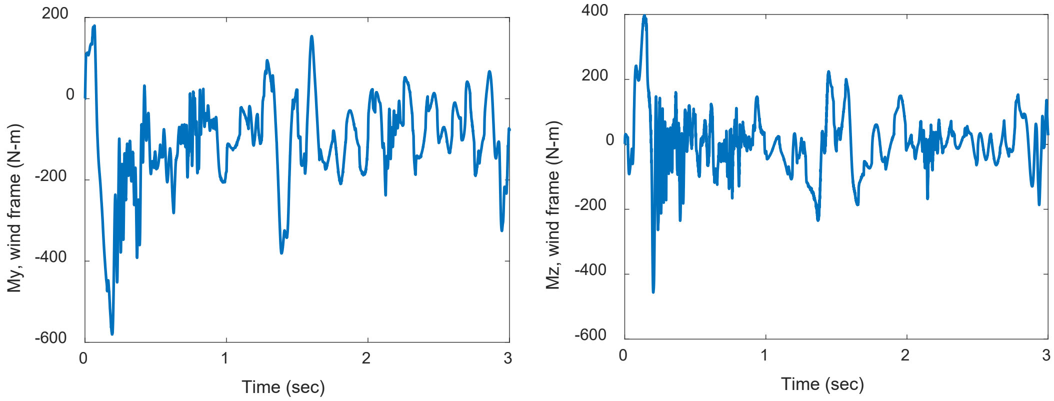

c) Pitch moment

d) Yaw moment

Fig. 7 Transverse force and moment components in the body frame, all actuators driven by orthogonal multisine staircase inputs, Mach = 0.99, $|\delta| = 20°$

Basic regression is easily applied when the predicted forces and moments are available. Essentially, it only requires rescaling the forces and moments to their nondimensional equivalents, choosing a vector of regressors, and applying least squares to solve for the underlying coefficients. Forces are divided by the dynamic pressure and reference area to render the coefficient form:

$$C_{Fi} = F_i/(\bar{q}\,S)\ . \tag{37}$$

Moments are divided by the dynamic pressure, reference area, and characteristic length:

$$C_{Mi} = M_i/(\bar{q}\,SD)\ . \tag{38}$$

Next, a set of regressors are chosen to reflect the terms in the AM expected to be dominant in the input/output path for the system identification scenario. The model should have a form such as

$$y = \beta_0 x_0 + \beta_2 x_1 + \beta_3 x_3 + \cdots + \beta_m \cdot 1\ , \tag{39}$$

where $\beta_0, \dots, \beta_{m-1}$ are unknown constants, $x_0, \dots, x_m$ are the regressors, and the final term β_m is a bias. Given Eq. 39 and data vector **y** of length > m, and matrix of regressors **X**, the least-squares estimate for the coefficient vector $\boldsymbol{\beta} = [\beta_0, \beta_1, \beta_2, \dots, \beta_m]$ can be found by[13]:

$$\boldsymbol{\beta} = (\mathbf{X}^T\mathbf{X})^{-1}(\mathbf{X}^T\mathbf{y}). \tag{40}$$

4.2 Regression for a Roll-Dependent Controlled Projectile

For the virtual fly-outs we choose the model:

$$\begin{aligned} C_\vartheta = {} & C^R_{\vartheta 1}(M, \phi_R) s_{\bar{\alpha}} + C^R_{\vartheta 2}(M, \phi_R) s^2_{\bar{\alpha}} + C^R_{\vartheta 3}(M, \phi_R) s^3_{\bar{\alpha}} + C^{M_1}_{\vartheta\delta}(M, \phi_1, \delta_1) \\ & + C^{M_1}_{\vartheta\delta}\left(M, \phi_1 + \frac{\pi}{2}, \delta_2\right) + C^{M_1}_{\vartheta\delta}(M, \phi_1 + \pi, \delta_3) + C^{M_1}_{\vartheta\delta}\left(M, \phi_1 + \frac{3\pi}{2}, \delta_4\right) \end{aligned} \tag{41}$$

In Eq. 41 there are five aerodynamic bank angles, one for the rigid aero surfaces and four for the moving aero surfaces, respectively. The MAS aero bank is related to the RAS by $\phi_1 = \phi_R + \pi/4$. Next, since we are estimating coefficients for the transverse terms only in a virtual environment, we expect the model to be perfectly symmetric; therefore, no forces or moments at zero AoA. Thus, there is no bias term. Finally, note that the same flap authority term $C^{M_1}_{\vartheta\delta}$ appears in each of the MAS terms. This is capitalizing on the facts presented in Eqs. 23 and 24. The consequence of this is that each regression will actually render four estimates of the coefficient $C^{M_1}_{\vartheta\delta}$ at four distinct phase angles. This is shown in Fig. 8 where four estimates of $C^{M_1}_{m0}$ from regression are shown over the full cycle prediction from the existing model.

One final note—the MAS terms in Eq. 41 correspond to table entries of the existing model for a specific flap deflection. Since the flaps in simulation move with a finite rise time, some samples of deflection will be less than the prescribed amplitude.

Thus, we divide each flap deflection history by the maximum deflection amplitude observed in each fly-out and fill the regression matrix with deflections as a portion of the max deflection. Thus, the final regressor matrix **X** for transverse forces is:

$$\mathbf{X} = \begin{bmatrix} s_{\bar{\alpha}}(t_1) & s_{\bar{\alpha}}^2(t_1) & s_{\bar{\alpha}}^3(t_1) & \boldsymbol{\delta_1}(t_1)/\bar{\delta} & \boldsymbol{\delta_2}(t_1)/\bar{\delta} & \boldsymbol{\delta_3}(t_1)/\bar{\delta} & \boldsymbol{\delta_4}(t_1)/\bar{\delta} \\ s_{\bar{\alpha}}(t_2) & s_{\bar{\alpha}}^2(t_2) & s_{\bar{\alpha}}^3(t_2) & \boldsymbol{\delta_1}(t_2)/\bar{\delta} & \boldsymbol{\delta_2}(t_2)/\bar{\delta} & \boldsymbol{\delta_3}(t_2)/\bar{\delta} & \boldsymbol{\delta_4}(t_2)/\bar{\delta} \\ & \vdots & & & \vdots & \vdots & \end{bmatrix} \tag{42}$$

and for moments it is:

$$\begin{bmatrix} \frac{\omega(t_1)D}{2V_\infty(t_1)} & s_{\bar{\alpha}}(t_1) & s_{\bar{\alpha}}^2(t_1) & s_{\bar{\alpha}}^3(t_1) & \boldsymbol{\delta_1}(t_1)/\bar{\delta} & \boldsymbol{\delta_2}(t_1)/\bar{\delta} & \boldsymbol{\delta_3}(t_1)/\bar{\delta} & \boldsymbol{\delta_4}(t_1)/\bar{\delta} \\ \frac{\omega(t_2)D}{2V_\infty(t_2)} & s_{\bar{\alpha}}(t_2) & s_{\bar{\alpha}}^2(t_2) & s_{\bar{\alpha}}^3(t_2) & \boldsymbol{\delta_1}(t_2)/\bar{\delta} & \boldsymbol{\delta_2}(t_2)/\bar{\delta} & \boldsymbol{\delta_3}(t_2)/\bar{\delta} & \boldsymbol{\delta_4}(t_2)/\bar{\delta} \\ & \vdots & & & & \vdots & \vdots & \end{bmatrix} \tag{43}$$

where the first column contains the angular velocity of the axis of interest ($\omega \in \{q, r\}$) scaled by the characteristic length D and the total velocity V_∞.

The post-flight data reduction is most easily explained by first looking at the expected form of the results. Figure 8 compares predictions of the zero AoA pitch moment due to a 20° deflection of MAS1 as a function of the aerodynamic bank with respect to MAS1. Since this is the zero AoA term, the aerodynamic bank is actually undefined; therefore, some explanation is in order before we proceed. Note in Fig. 4a that the aerodynamic bank defines the angular relationship between the vehicle and the wind frame. For this example in particular, when the aerodynamic bank is zero, the wind frame pitch moment unit vector $\hat{m}$ will be aligned with MAS1. Thus, the pitch moment due to MAS1 will be at a maximum in the wind frame when the aerodynamic bank is zero or π radians. The pitch moment generated in the MAS1 frame will be projected onto the $\hat{m}$ and $\hat{n}$ directions in the wind frame for aero bank angles other than zero and π. In Fig. 8, this is evident as the zero AoA moment due to flap 1 varies as a fundamental harmonic with period 2π.

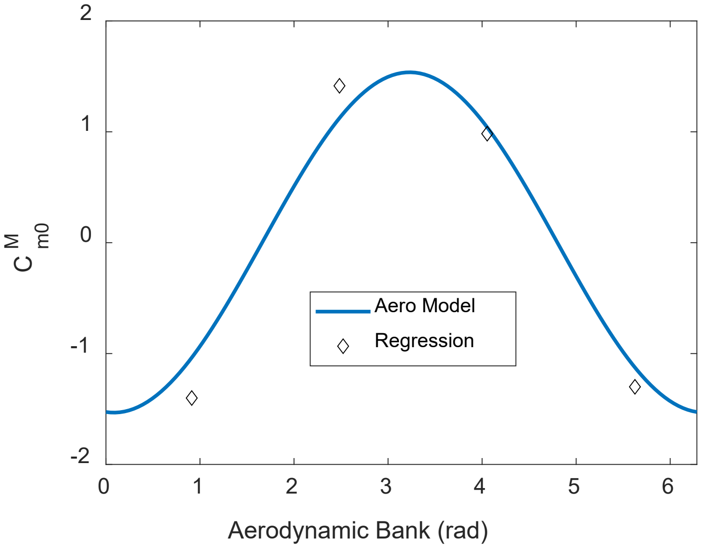

Fig. 8 Zero AoA pitch moment prediction for MAS 1. Baseline AM shown as solid blue line. Points from regression at a single bank angle shown as black diamonds.

Because we wish to capture the aerodynamic bank dependency of the flap authority coefficients ($C_{N0}^{M_1}, C_{S0}^{M_1}, C_{m0}^{M_1}, C_{n0}^{M_1}$), we will subdivide the post-flight data into sets with a common aerodynamic bank. The baseline AM was formed from several data sources, the most comprehensive of which uses a grid of 32 aerodynamic bank angles or every 11.25° around the roll cycle. After some trial and error, we determined that using 16 distinct bank angles gave the best balance between the number of estimates along the bank axis and the conditioning of each estimate.

Since the aero bank varies continuously during the simulation, we use the MATLAB histogram tool to sort all of the data into bins that are equally spaced in aero bank. The histogram tool determines the bin edges and plots the frequency of samples in each bin based on the user-specified number of bins. These edge values will vary somewhat between fly-outs; therefore, we use the tool with each fly-out to determine the bin edges. A sample histogram of aero bank angles for a fly-out with 6000 total time steps is shown in Fig. 9.

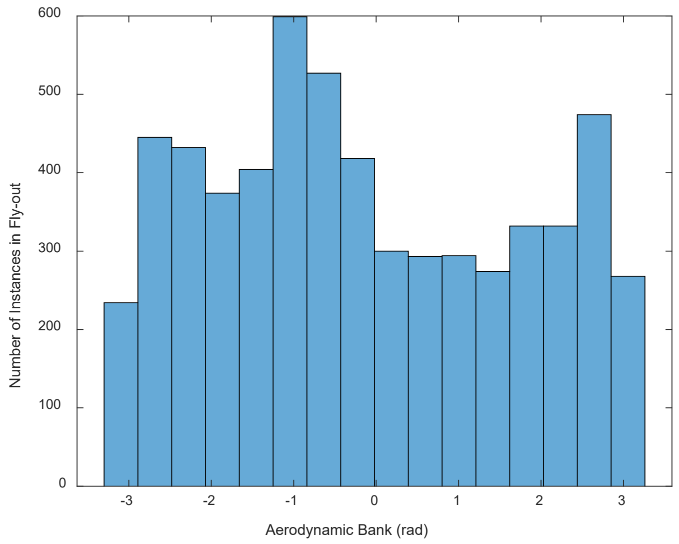

Fig. 9 Sample histogram from fly-out aero bank data

Once the bin edges are determined, they are used to down-select 16 corresponding subsets of the $\mathbf{X}$ matrix (Eqs. 42 and 43), and the corresponding rows of force/moment coefficient predictions in $\mathbf{y}$. Equation 36 is then used to find the least-squares estimates of the seven coefficieints for force terms, or eight for moment terms. Thus, for each fly-out, 16 estimates are rendered at 16 aero bank angles for each of 7 or 8 coefficients. Four of these coefficients are actually duplicates of one another at different phase angles (recall Eq. 41); therefore, we in fact have 64 total estimates of the flap influence on each transverse force/moment at zero AoA.

The estimated rigid aero surface coefficients are ignored in this study as our goal is to better predict the flap control authority. Since we have 64 estimates of $C_{\vartheta\delta}^{M_1}$ as a function of 64 aero bank angles, we will compute and plot a few more quantities to complete the analysis.

Figure 10 shows the baseline AM prediction and all 64 regression estimates of transverse forces/moments at 0.99 Mach with a maximum deflection of 20°. The blue lines are the baseline AM predictions. It is immediately evident that the regression results match the trend of the existing model—namely, varying in amplitude as a single harmonic with period equal to the roll cycle. The red line is formed by finding the single harmonic of period 2π that fits the regression estimates best in a least-squares sense. This is a way of quantifying the regression results in terms of amplitude and phase. Since we seek a global set of corrections to the baseline model, we want each force/moment term to be represented by a single quantity (if possible) at each Mach-deflection pair. We further note that the phase differences between the AM and best-fit harmonic are very small. Thus, we will keep only the best-fit harmonic amplitude at each Mach-deflection pair to use in correcting the global model.

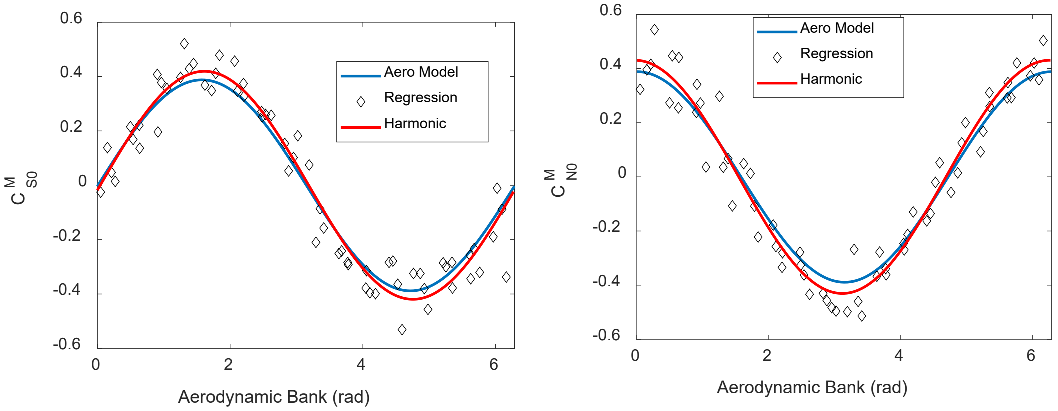

a) Side force **b) Normal force**

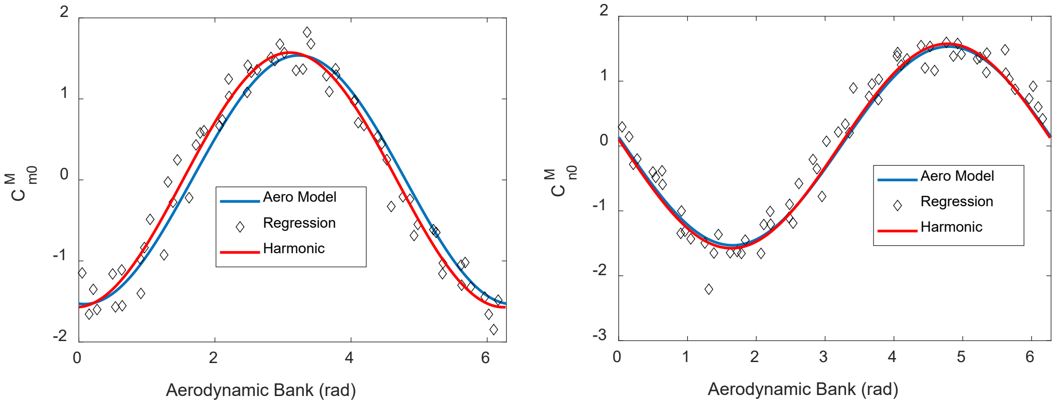

c) Pitch moment **d) Yaw moment**

Fig. 10 Comparison: baseline AM, regression estimates at 16 aerodynamic bank angles for all four actuators, and single harmonic best fit to regression estimates

4.3 Global Model Meta-Analysis

The end goal of this study is to tune the global set of flap authority coefficients to better match the performance observed in the coupled study. Thus, we collect as many fly-outs as practical considering the heavy computation load of a single fly-out (~100 wall clock hours per 3-s flight). The initial set of experiments was selected using a rank-one lattice technique[14,15] to determine the minimal set of Mach-deflection pairs that best spanned the search space. This set is illustrated in Fig. 11. The Mach-deflection search space was limited to $0 < \delta < 20°$ and $0 < M < 4.0$. These limits were determined by running the fly-out in a low-fidelity, 6-DOF simulation and observing whether the vehicle remained within the nominal flight envelope (did not tumble) for the full 3-s flight.

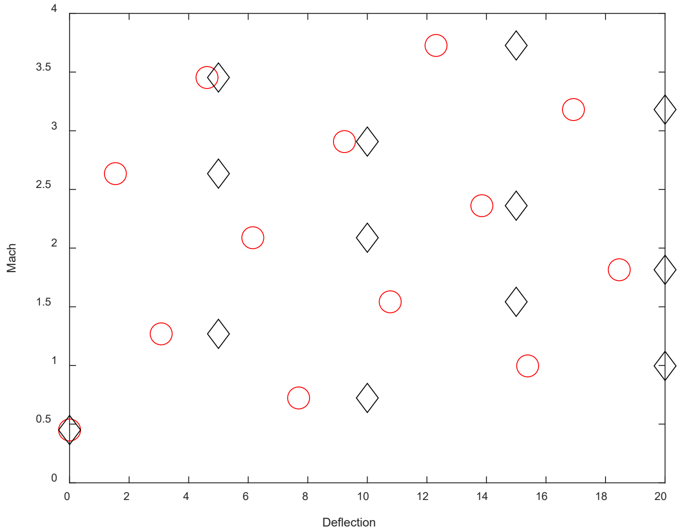

Fig. 11 Rank-one lattice design of flight conditions for global design of experiments. Red circles are 13 lattice points spanning the Mach/deflection space. Black diamonds are equal in Mach with deflections rounded up to the nearest 5°.

Figure 11 shows the result of the rank-one lattice design of experiments. The lattice generated 13 possible flight conditions as shown by the red circles. The case at $M = 0.5$, $\delta = 0$ was discarded since the goal is to observe flight with nonzero deflections. The deflections were rounded up to the nearest 5° for the remaining cases, since the goal is to tune a table as described in Section 4.3. The points tested are shown as black diamonds in Fig. 11.

All 12 flight conditions were bench tested in the low-fidelity, 6-DOF prior to deployment in the high-performance computing (HPC) environment since each virtual fly-out required 100 h and used hundreds of cores.

The data reduction of each individual fly-out resulted in a set of four amplitudes for the transverse force/moment prediction models as shown in Section 4.2. In Fig. 12, we juxtapose each set of 12 amplitude estimates in Mach-deflection space over the corresponding surface of amplitudes from the baseline AM. The corresponding data is also shown in Table 1. On average, the force predictions from the system ID are 15% larger than those from the AM with the largest difference.

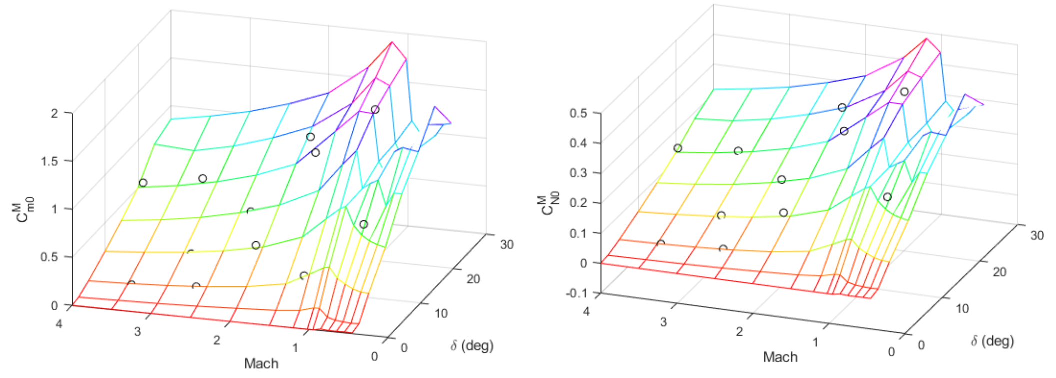

a) Pitch moment **b) Normal force**

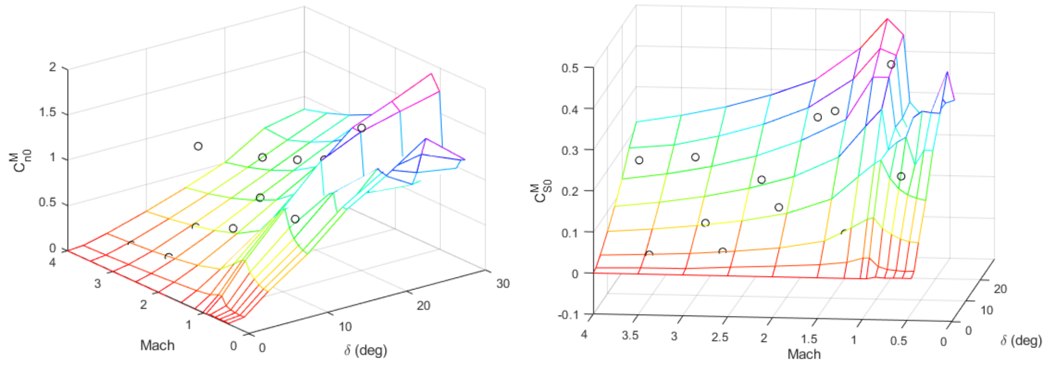

c) Yaw moment **d) Side force**

Fig. 12 Comparison between baseline AM max amplitude and results of the 12 coupled simulation fly-outs for the transverse flap authority zero AoA terms

Table 1 Experiment and model determined amplitudes

Mach, delta	C_{S0} Experiment	C_{S0} Model	C_{N0} Experiment	C_{N0} Model
0.72,10	0.1992	0.1688	0.21079	0.16927
0.99,20	0.41951	0.38792	0.43071	0.38855
1.27,5	0.083303	0.097523	0.073156	0.097618
1.54,15	0.3289	0.21729	0.34213	0.21782
1.81,20	0.28716	0.22991	0.35044	0.23103
2.09,10	0.11781	0.10323	0.11202	0.10357
2.36,15	0.15821	0.13673	0.15211	0.13751
2.63,5	0.032641	0.034518	0.032874	0.034383
2.91,10	0.075707	0.069153	0.074686	0.069069
3.18,20	0.18385	0.16215	0.15903	0.16268
3.45,5	0.021559	0.022142	0.021715	0.021925
3.73,15	0.1992	0.1688	0.21079	0.16927

Table 1 Experiment and model determined amplitudes (continued)

Mach, delta	C_{l0} Ex	C_{l0} Model	C_{m0} Ex	C_{m0} Model	C_{n0} Ex	C_{n0} Model
0.72,10	0.0947	0.1182	0.75982	0.64516	0.86641	0.64574
0.99,20	0.1673	0.2523	1.5715	1.5366	1.5757	1.5326
1.27,5	0.0509	0.0581	0.358	0.38363	0.22182	0.38422
1.54,15	0.1236	0.1474	1.2574	0.86567	1.2154	0.86831
1.81,20	0.1415	0.1849	1.2188	0.92127	1.0368	0.92163
2.09,10	0.0709	0.0679	0.42613	0.41568	0.45114	0.41622
2.36,15	0.1012	0.1034	0.57402	0.54976	0.61058	0.54982
2.63,5	0.0233	0.0209	0.12901	0.14242	0.12401	0.14234
2.91,10	0.0499	0.0503	0.26968	0.2793	0.27636	0.27969
3.18,20	0.1058	0.1118	0.67062	0.6522`	0.75046	0.65432
3.45,5	0.0145	0.0154	0.080384	0.090744	0.070824	0.092219
3.73,15	0.0947	0.0659	0.75982	0.64516	0.86641	0.64574

In Fig. 12, absolute values are plotted for the moment terms (positive deflections create negative moments in the specified frames). The surface and points for pitch and yaw are nearly identical when viewed this way because of symmetry. The normal and side force data shown are also nearly identical. This confirms the second corollary to the original modeling assumptions.[5] We have included all four plots to give two perspectives of the surface in 3-D. Finally, note the large ridge in the AM surface at transonic (M = 1) speeds. The rank-one lattice method of choosing flight conditions ignored the fact that aerodynamic forces and moments tend to have large variations near Mach 1. Unfortunately, this resulted in picking only one subsonic point: $(M, \delta) = (0.723, 10°)$, and only two transonic points: $(M, \delta) = \{(0.996, 20°)$ and $(1.269, 5°)\}$. This lack of data on the "ridge" will make it difficult to provide more than a global correction in bias. Our primary goal in performing these computational experiments is to tune the flap authority model over the flight envelope. In Section 4.4, we explore the use of kriging and cokriging to provide the best possible outcome.

4.4 Kriging and Cokriging

4.4.1 Kriging

Kriging is a statistical interpolation method introduced first in the mining community by Krige.[16] It has come into recent prominence in the aerodynamic modeling and aerospace multidisciplinary design communities. One of the most accessible treatments of kriging and cokriging is by Forrester et al.[17] We rely on their notation here as modified by Bailly and Bailly.[18] Kriging is closely related to the radial basis function (RBF) in machine learning, and relies on spatial correlation between *n* sample points $(\boldsymbol{X_1}, \ldots, \boldsymbol{X_n})$ for which the function values have been found $(\boldsymbol{Y_1}, \ldots, \boldsymbol{Y_n})$. The kriging model is a Gaussian process with covariance given as

$$\mathbf{Cov}(\boldsymbol{X_i}, \boldsymbol{X_j}) = \sigma^{\mathbf{2}} \boldsymbol{R}(\boldsymbol{X_i}, \boldsymbol{X_j}\colon \boldsymbol{\theta}), \tag{44}$$

where $\sigma^{\mathbf{2}}$ is the variance of the process and $\boldsymbol{R}$ is a correlation function with hyperparameters $\boldsymbol{\theta}$. Typically, and in this report, the Gaussian (RBF) kernel is preferred

$$\boldsymbol{R}\left(\boldsymbol{X_i}, \boldsymbol{X_j}\colon \boldsymbol{\theta}\right) = \exp\left[-\left\|\boldsymbol{\theta} \cdot \left\|\boldsymbol{X_i} - \boldsymbol{X_j}\right\|_2^{\boldsymbol{p}}\right\|_1\right], \tag{45}$$

where $\|.\|_2$ indicates the Euclidean norm and $\|.\|_1$ indicates the *taxicab* norm. Since $\boldsymbol{\theta}$ is a vector of positive constants, $\boldsymbol{R}\left(\boldsymbol{X_i}, \boldsymbol{X_j}\colon \boldsymbol{\theta}\right) \leq 1, \forall\,(i,j)$, the hyperparameters consist of $(\boldsymbol{\theta}, \boldsymbol{p})$, which may both have differing values in each dimension. In this report, we choose $\boldsymbol{p} = 2$ for all dimensions and solve for the best $\boldsymbol{\theta}$ by maximizing the likelihood function:

$$L = -\frac{N}{2}\ln(\sigma^2) - \frac{1}{2}\ln(\det(\boldsymbol{R}))\,. \tag{46}$$

We use a genetic algorithm to determine the set of best $\boldsymbol{\theta}$ for each surface representing a particular force/moment coefficient (Fig. 13).

The kriging prediction is the unbiased maximum likelihood estimate given by

$$\hat{Y}(\boldsymbol{X}) = \mu_Y + \boldsymbol{r}^{\mathrm{T}}(\boldsymbol{X})\boldsymbol{R}^{-1}(\boldsymbol{Y_c} - \mathbf{1}\mu_Y)\,, \tag{47}$$

where $\boldsymbol{r}(\boldsymbol{X})$= $\boldsymbol{R}\left(\boldsymbol{X}, \boldsymbol{X_j}\colon \boldsymbol{\theta}\right), j = 1, \ldots, n$ (i.e., a column vector), $\mu_Y = \mathbf{1}^T\boldsymbol{R}^{\mathbf{-1}}\boldsymbol{Y_c}/(\mathbf{1}^T\boldsymbol{R}^{-1}\mathbf{1})$, and $\mathbf{1}$ is an $n \times 1$ column vector of ones.

4.4.2 Cokriging

Cokriging is a well-established method to increase the fidelity of a low-cost predictor by adjusting its output to match a sparse set of high-fidelity predictions. The general idea is that the high-cost predictions can be modeled by scaling the low-cost predictions by a factor ρ and adding a second Gaussian process (RBF) $\boldsymbol{Z_d}$:

$$\boldsymbol{Z}_e(\boldsymbol{X}) = \rho \boldsymbol{Z}_c(\boldsymbol{X}) + \boldsymbol{Z}_d(\boldsymbol{X}). \tag{48}$$

To find the second model there must be some overlap in the underlying data sets and typically $\boldsymbol{X_e} \subset \boldsymbol{X_c}$. A combined covariance matrix is built as:

$$\boldsymbol{C}(\boldsymbol{X_c}, \boldsymbol{X_e} \colon \boldsymbol{\theta_c}, \boldsymbol{\theta_d}) = \begin{bmatrix} \sigma_c^2 \boldsymbol{R_c}(\boldsymbol{X_c}, \boldsymbol{X_c}) & \rho \sigma_c^2 \boldsymbol{R_c}(\boldsymbol{X_c}, \boldsymbol{X_e}) \\ \rho \sigma_c^2 \boldsymbol{R_c}(\boldsymbol{X_e}, \boldsymbol{X_c}) & \rho^2 \sigma_c^2 \boldsymbol{R_c}(\boldsymbol{X_e}, \boldsymbol{X_e}) + \sigma_d^2 \boldsymbol{R_d}(\boldsymbol{X_e}, \boldsymbol{X_e}) \end{bmatrix}, \tag{49}$$

where the subscripts (c, d) indicate which set of hyperparameters are used to form that particular quantity. The low-fidelity hyperparameters are found by kriging the low-fidelity data as shown in Section 4.4.1. To determine the hyperparameters for the high-fidelity set, difference data is found from the overlapping samples:

$$\boldsymbol{d} = \boldsymbol{y}_e - \rho \boldsymbol{y}_{\mathrm{c}}(\boldsymbol{X_e})\ . \tag{50}$$

And, maximizing the updated likelihood function:

$$L = -\frac{N_e}{2} \ln(\sigma_d^2) - \frac{1}{2} \ln(\det(\boldsymbol{R_d}(\boldsymbol{X_e}, \boldsymbol{X_e})))\ . \tag{51}$$

The cokriging maximum likelihood predictor is then given by

$$\hat{Y}_e(\boldsymbol{X}) = \mu_Y + \boldsymbol{c}^{\mathrm{T}}(\boldsymbol{X}) \boldsymbol{C}^{-1} (\boldsymbol{Y} - \boldsymbol{1}\mu_Y) \tag{52}$$

where

$$\mathbf{c} = \begin{bmatrix} \rho \sigma_c^2 R(\boldsymbol{X}, \boldsymbol{X_c} \colon \boldsymbol{\theta_c}) \\ \rho^2 \sigma_c^2 R(\boldsymbol{X}, \boldsymbol{X_e} \colon \boldsymbol{\theta_c}) + \sigma_d^2 R(\boldsymbol{X}, \boldsymbol{X_e} \colon \boldsymbol{\theta_d}) \end{bmatrix} \tag{53}$$

and $\boldsymbol{Y} = [\boldsymbol{Y_c^T} \quad \boldsymbol{Y_e^T}]^{\boldsymbol{T}}$, $\mu_Y = \boldsymbol{1}^T \boldsymbol{C}^{-1} \boldsymbol{Y} / (\boldsymbol{1}^T \boldsymbol{C}^{-1} \boldsymbol{1})$.

4.4.3 Results of Cokriging the Coupled System ID Data with Existing Aero Database

To prepare for the cokriging step, a kriging model $\boldsymbol{Z_c}(\boldsymbol{X})$ is formed by sampling the maximum force/moment due to flap deflection along each axis (side, normal, pitch, yaw) from the existing AM using an equally spaced 15×15 grid in $0.5 \leq M \leq 4, 2° \leq \delta \leq 20°$ space. This model is validated against the AM, then used to predict $\boldsymbol{y}_{\mathrm{c}}(\boldsymbol{X_e})$—the model predictions at the high-fidelity data points—as shown. Cokriging is then applied to the 13 data points from the virtual fly-outs using Eqs. 48, 50, and 51. The resulting Gaussian process models are used to predict a 14×4 grid of updated estimates in the range $0.45 \leq M \leq 4, 5° \leq \delta \leq 20°$ using Eqs. 49, 52, and 53 as illustrated in the following.

Figures 13 and 14 show the result of cokriging results of coupled system ID runs for 13 flight conditions. These include the 12 listed in Table 1. Since the response surfaces typically have a steep ridge at high deflection near Mach 1 with a deep ridge in the adjacent subsonic region, a 13th flight condition was included at $(M, \delta) = (1.2, 20°)$. The plot in Fig. 13 typifies the overall results, except that we have plotted the roll authority without taking the magnitude thereof. The existing aero database, which was determined using the Cart3D inviscid CFD tool, is shown as a solid surface. The coupled system ID data are shown as red asterisks. The cokriging prediction is shown as a semitransparent surface with black mesh. Since positive flap deflections cause negative roll moments, the "ridge" at Mach 1 is a deep trough in the solid surface. The largest deflections are in the foreground, and it is apparent that Cart3D overpredicts flap roll authority in the transonic region. The data at Mach 0.99 and Mach 1.2 have a much smaller magnitude than the corresponding Cart3D predictions. Cokriging seeks to preserve the overall shape of the low-fidelity model (Cart3D) while matching the high-fidelity predictions (coupled CFD++). In this case the surfaces match reasonably well, and the transonic trough retains its shape, save for the region near the system ID predictions.

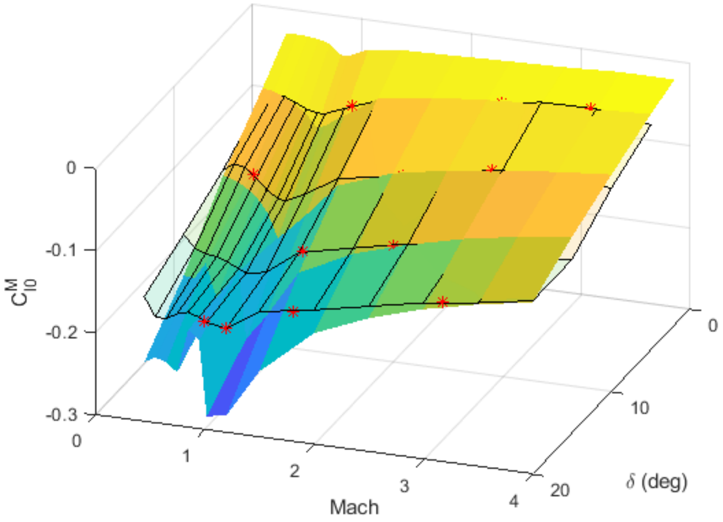

Fig. 13 **Result of cokriging the flap roll authority C^M_{l0}. Asterisks and black mesh are the system ID estimates and cokriging surface, respectively. Solid surface is the baseline AM formed from Cart3D.**

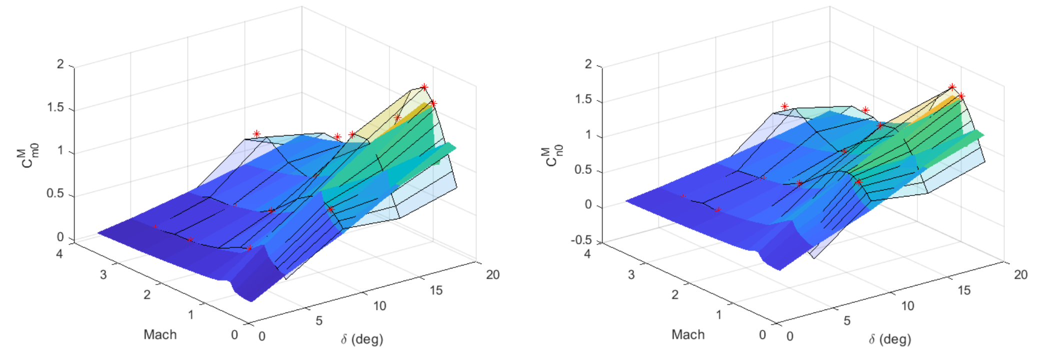

a) Pitch moment **b) Yaw moment**

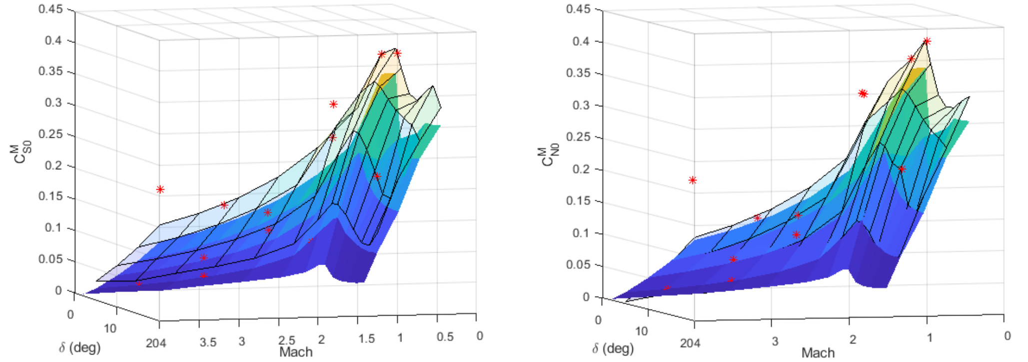

c) Side force **d) Normal force**

Fig. 14 Result of cokriging system ID (transparent) results against existing AM (solid)

Figure 14 shows the cokriging results for the transverse forces and moments. A great deal of symmetry is expected since the forces and moments are predicted in the wind frame. That means over a roll cycle, a single flap deflection will exert a force that is resolved into both side and normal forces, and the peak contribution will occur when this force is aligned with one of the aforementioned axes. The same logic results in expecting pitch and yaw moment peak contributions to be symmetric as well.

All results in Fig. 14 share one common feature—the existing AM apparently underpredicts the flap force and moment contributions at high deflections near Mach = 1. The cokriging model compensates for this by lifting the highest part of the Mach 1 ridge (large deflections) up to the system ID estimates. Due to the sparsity of subsonic system ID data (one point), the cokriging surface largely matches the shape of the existing AM; however, the trough in the subsonic region is not nearly as deep. Note that the kriging and cokriging models are trained in the domain $5° \leq \delta \leq 20°$ and as such cannot extrapolate beyond these bounds. The existing AM is plotted using $2° \leq \delta \leq 20°$ to show trends of the underlying surfaces in the foreground.

The point at $(M, \delta) = (3.73, 15°)$ has little influence on the normal and side force cokriging results. It seems that other high-fidelity predictions in the vicinity cause it to consider this point as an outlier. On the moment plots, the point at $(M, \delta) = (3.18, 20°)$ is also significantly higher than the existing model; therefore, the cokriging surfaces rise to meet both.

5. Conclusion

This report shows how a high-fidelity, coupled CFD/RBD simulation was used to determine the zero AoA flap authority terms in an AM. A rank-one lattice technique was used to find 12 flight conditions that spanned the search space. At each flight condition, four independent flap deflection commands were determined using orthogonal multisine staircase functions. This allowed all four surfaces to move simultaneously during the virtual fly-out yet provide a response that is separable and observable for post-flight regressions. Due to the strong roll dependence of flap authority, input deflections and predicted forces were subdivided into 16 cases based upon the vehicle aerodynamic bank. Regressions were performed on each subset for the four transverse force/moment terms, resulting in 64 total estimates of each over a full roll cycle. These estimates were plotted, and a best-fit harmonic was found to capture the overall trend of each in a single amplitude at the fly-out Mach and deflection.

The trend observed over a full roll cycle confirmed a fundamental assumption in the baseline AM that the force/moment contribution from a single flap could be predicted over the full roll cycle from zero roll predictions of the transverse components. The experiment was repeated at 12 flight conditions designed to span the Mach/deflection envelope for subsonic to high supersonic flight with small-to-moderate defections. At each flight condition, the best-fit harmonic amplitudes were collected and compared to the baseline AM predictions. The regressions at all 12 flight conditions bear out 2 essential corollaries to the fundamental modeling assumption that a) the flap force/moment contribution along a transverse axis resembles a single harmonic with a distinct amplitude, and b) this amplitude is shared (symmetric) between force components (*S*, *N*) and between moment components (*m*, *n*) for a specific flap deflection δ.

The single harmonic amplitudes found from regression were used to update the corresponding amplitudes from the baseline AM using cokriging. Cokriging combines a Gauss process model and a low-cost, low-fidelity model with a second model formed from the difference between the low-fidelity model and a higher-fidelity model. It is able to use a very sparse sampling of the high-fidelity model to tune the low-fidelity model to match the high-fidelity one, as long as the samples span the input space. Since we chose the 12 flight conditions to adequately span the space, cokriging rendered updated response surfaces for the five force/moment quantities of interest that matched the amplitudes found from the computational experiment while generally preserving the response surface shapes of the baseline model. Since the response surface shapes were largely preserved during this tuning, we conclude that the baseline model was correct in assuming that combined flap contributions could be predicted from the force/moment contribution from a single flap. This also confirms the two corollaries previously mentioned.

6. References

1. Mann FW. The bullet's flight from powder to target. Munn & Co.; 1909.
2. Dodson MG. An historical and applied aerodynamic study of the Wright brothers' wind tunnel test program and application to successful manned flight. US Naval Academy; 2005. Trident Scholar Project Report No.: 334.
3. Sahu J, Burchett B, Gruenwald B. Advanced CFD-based coupled computational approach for prediction of complex flight behaviors. ICCFD11; 2022 July 11–15; Maui, HI.
4. Sahu J, Gruenwald B, Burchett B. Adaptive control validation using a MATLAB-based CFD/RBD coupled simulation. AIAA Aviation Forum; 2022 June 27 – July 1; Chicago, IL.
5. Vasile J, Bryson J, Sahu J, Paul J, Gruenwald B. Aerodynamic data set generation of a long range projectile. DEVCOM Army Research Laboratory (US); 2020 Aug. Report No.: ARL-TR-9019.
6. Pokela R, Kumar R, Vasile J. Experimental and computational aerodynamic characterization of a generic high-speed projectile configuration. AIAA Aviation Forum; 2021 Aug.
7. Burchett B, Vasile J, and Bryson J. Combining sparse and dense databases to form a robust aerodynamic model for a long-range high-speed projectile. DEVCOM Army Research Laboratory (US); 2021 July. Report No.: ARL-TR-9235.
8. Morelli EA. Practical aspects of multiple-input design for aircraft system identification flight tests. AIAA Aviation Forum; 2021 Aug 2–6; Virtual Event.
9. Peroomian O, Chakravarthy S, Goldberg U. A 'grid-transparent' methodology for CFD. AIAA; 1997. AIAA Paper No.: 97-07245.
10. Peroomian O, Chakravarthy S, Palaniswamy S, Goldberg U. Convergence acceleration for unified-grid formulation using preconditioned implicit relaxation. AIAA; 1998. AIAA Paper No.: 98-0116.
11. Goldberg UC, Peroomian O, Chakravarthy S. A wall-distance-free K-E model with enhanced near-wall treatment. ASME J Fluids Eng. 1998;120:457–462.

12. Sahu J, Gruenwald B, Burchett B. Adaptive control validation using a MATLAB-based CFD/RBD coupled simulation. DEVCOM Army Research Laboratory (US); 2022 Apr. Report No.: ARL-TR-9433.

13. Allen J, Ghoreyshi M. Forced motions design for aerodynamic identification and modeling of a generic missile configuration. Aerospace Sci Tech. 2018;77:742–754.

14. Lyu Y, Yuan Y, Tsang I. Subgroup-based rank-1 lattice quasi-Monte Carlo. 34th Conference on Neural Information Processing Systems (NeurIPS 2020), Vancouver, Canada.

15. Huang H, Giacobello M. Uncertainty quantification in store separation analysis using Kestrel, design of experiments, and surrogate modelling. AIAA SciTech Forum; 2022 Jan 3–7; San Diego, CA.

16. Krige DG. A statistical approach to some basic mine valuation problems in the Witwatersrand. Journal of the Chemical, Metallurgical, and Mining Society of South Africa. 1951;52(6):119–139.

17. Forrester A, Sobester A, Keane A. Multi-fidelity optimization via surrogate modeling. Proceedings of the Royal Society of London, Series A: Mathematical and Physical Sciences. 2007 Dec;463(2088):3251–3269.

18. Bailly J, Bailly D. Multifidelity aerodynamic optimization of a helicopter rotor blade. AIAA Journal. 2019;57(8):3132–3144.

Appendix. Rank-One Lattice Design of Experiments

To generate *n* test points that span a *d* dimensional space, the *j*th test point is given as (Lyu et al.[1]):

$$\boldsymbol{y}_j = \frac{(j \cdot \mathbf{z}) \bmod n}{n}, j \in \{0, 1, \dots, n-1\}, \tag{A-1}$$

where the generating vector is given by

$$\mathbf{z} = \begin{bmatrix} g^0 & g^{\frac{n-1}{2d}} & g^{\frac{2(n-1)}{2d}} & \dots & g^{\frac{(d-1)(n-1)}{2d}} \end{bmatrix} \cdot \bmod n, \tag{A-2}$$

and g is a primitive root of *n*.

For the 2-D search space in (δ, Mach) the entire design of experiment is found in just a few lines of MATLAB code:

```
d = 2;
n = 13;
g = 2; % primitive root of n

for k = 1:d
 z(k,1) = mod(g^((k-1)*(n-1)/(2*d)),n);
end

y = mod(z*(0:n-1),n)*(1/n);

% scale to degrees, & 0.45 < Mach < 4, round deflection to nearest 5 deg:
y(1,:) = 5*(ceil(4*y(1,:)));
y(2,:) = (4 - 0.45)*y(2,:) + 0.45;
```

The circles plotted in Fig. 11 were rendered by this code without the rounding provided by “ceil.” The diamonds were rendered using the full code including “ceil.”

---

[1] Lyu Y, Yuan Y, Tsang I. Subgroup-based rank-1 lattice quasi-Monte Carlo. 34th Conference on Neural Information Processing Systems (NeurIPS 2020); 2020; Vancouver, Canada.

List of Symbols, Abbreviations, and Acronyms

2-/3-D	two-/three-dimensional
6-DOF	six-degrees-of-freedom
AM	aerodynamic model
AoA	angle-of-attack
ARL	Army Research Laboratory
CFD	computational fluid dynamics
cg	center of gravity
DEVCOM	US Army Combat Capabilities Development Command
FCS	flight control system
HPC	high-performance computing
ID	identification
MAS	moveable aerodynamic surface
RANS	Reynolds-averaged Navier–Stokes
RAS	rigid aerodynamic surface
RBD	rigid body dynamics
RBF	radial basis function
RPF	relative peak factor
WT	wind tunnel
$\{x,y,z\}$	projectile cg position in gun tube frame [m]
$\{V_x, V_y, V_z\}$	projectile cg velocity in gun tube frame [m/s]
$\{\phi, \theta, \psi\}$	projectile roll, pitch, and yaw in gun tube frame [rad]
$\{u,v,w\}$	projectile linear velocity in the body or no-roll frame [m/s]
$\{p,q,r\}$	projectile angular rates in the body or no-roll frame [rad/s]
$\{X,Y,Z\}$	total force vector in projectile body frame [N]
$\{L,M,N\}$	total moment vector in projectile body frame [N-m]
m	projectile mass [kg]
$\mathbf{T}$	rotation matrix
$\mathbf{S}$	skew matrix for cross product
$\mathbf{I}$	inertia matrix [kg-m^2] or identity matrix

V	total velocity $\sqrt{u^2 + v^2 + w^2}$ [m/s]
ρ	atmospheric density [kg/m^3]
S	area of projectile cross section [m^2]
s	arclength traveled [cal.]
D	projectile diameter [m]
$C_{N0}^{M_i}$	normal force due to MAS i deflection at zero AoA
$C_{m0}^{M_i}$	pitch moment due to MAS i deflection at zero AoA
$C_{l0}^{M_i}$	roll moment coefficient due to MAS i deflection at zero AoA
$C_{S0}^{M_i}$	side force due to MAS i deflection at zero AoA
$C_{n0}^{M_i}$	side moment due to MAS i deflection at zero AoA

Subscript

$b2i$	ground to body frame
$b2e$	body to Euler frame
ϑ	placeholder for force moment terms

Superscript

T	matrix transpose
M	MAS term

1	DEFENSE TECHNICAL
(PDF)	INFORMATION CTR
	DTIC OCA
1	DEVCOM ARL
(PDF)	FCDD RLD DCI
	TECH LIB
10	DEVCOM ARL
(PDF)	FCDD RLW LE
	L STROHM
	VA BHAGWANDIN
	J BRYSON
	B BURCHETT
	I CELMINS
	J DESPIRITO
	LD FAIRFAX
	B GRUENWALD
	J PAUL
	JD VASILE